arXiv:1601.04496v1 [math.NA] 18 Jan 2016

# A modified algebraic reconstruction technique taking refraction into account with an application in terahertz tomography

Jens Tepe*, Thomas Schuster† and Benjamin Littau‡

**Key words and phrases.** terahertz tomography, nondestructive testing, algebraic reconstruction technique (ART), reflection losses, refractive index, Snell's law

## Abstract

Terahertz (THz) tomography is a rather novel technique for nondestructive testing that is particularly suited for the testing of plastics and ceramics. Previous publications showed a large variety of conventional algorithms adapted from computed tomography or ultrasound tomography which were directly applied to THz tomography. Conventional algorithms neglect the specific nature of THz radiation, i. e. refraction at interfaces, reflection losses and the beam profile (Gaussian beam), which results in poor reconstructions. The aim is the efficient reconstruction of the complex refractive index, since it indicates inhomogeneities in the material. A hybrid algorithm has been developed based on the algebraic reconstruction technique (ART). ART is adapted by including refraction (Snell's law) and reflection losses (Fresnel equations). Our method uses a priori information about the interface and layer geometry of the sample. This results in the "Modified ART for THz tomography", which reconstructs simultaneously the complex refractive index from transmission coefficient and travel time measurements.

## 1 Introduction

Terahertz (THz) radiation has become increasingly popular for nondestructive testing of plastics and ceramics in recent years. With a frequency range between 100 GHz to 10 THz, this radiation is situated between microwaves and infrared light within the electromagnetic spectrum. Thus, in terms of the wavelength, THz radiation shows elements of ray character (X-ray CT) as well as of wave character (ultrasound tomography). As a result, the wave character cannot be completely neglected. While plastics and ceramics are almost transparent in this frequency range, THz radiation cannot easily penetrate water, metals and conductive materials. Because of its relatively long wave length compared to X-rays, THz radiation has a limited lateral resolution. However, by using modulated THz radiation, information about both phase and amplitude are available as measured data in contrast to conventional tomographic methods [21].

The inverse problem of THz tomography consists of determining dielectric properties (i. e. refractive index $n$ and absorption coefficient $\alpha$) of the material from phase and amplitude information of the THz radiation, which admits finding material characteristics such as filler content or the detection of cracks and air cavities. For an overview on the relatively new field of tomographic methods using THz radiation, see Wang et al. [34], Guillet et al. [17] and Ferguson [14, 15]. Published results can be divided into transmission or reflection tomographic methods

*Department of Mathematics, Saarland University, PO Box 15 11 50, 66041 Saarbrücken, Germany (jens.tepe@num.uni-sb.de)

†Department of Mathematics, Saarland University, PO Box 15 11 50, 66041 Saarbrücken, Germany (thomas.schuster@num.uni-sb.de), correspondent author.

‡German Plastics Center, 97076 Würzburg, Germany (b.littau@skz.de)

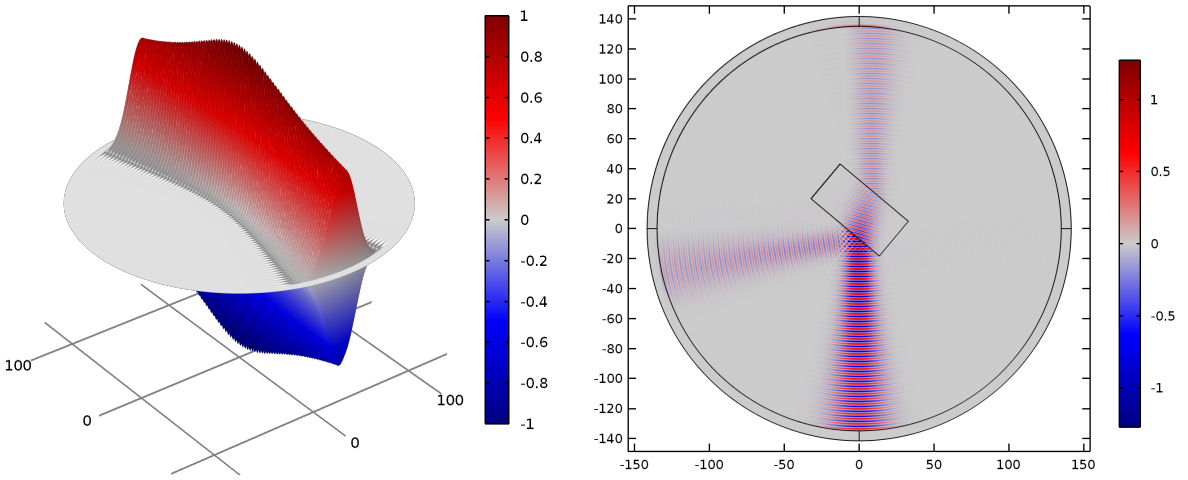


(a) 3D representation of the Gaussian beam

(b) Simulation of the electric field of an object consisting of polyethylene ($\tilde{n} = 1.51 + 0.023i$)

Figure 1: THz radiation for $f = 90\,\text{GHz}$ propagating from bottom to top as a simulation based on the Helmholtz equation

based on the available measured data. The adaption of computed tomography methods [20, 25] to the THz range is widely distributed [7, 13, 15, 18, 26, 34]. Here a very simplified propagation along straight lines is used with the Radon transform as mathematical model. However, physical effects such as refraction, diffraction, edge effects and the Gaussian beam profile have an influence on THz measurements [8]. Some publications consider these effects by adaptations. In [29], Recur et al. presented a filtered backprojection and adapted iterative methods (SART, OSEM) for 3D THz CT, which considers the intensity distribution of THz rays (Gaussian beam). Mukherjee et al. only regard cylindric objects, but take Fresnel reflection losses and beam steering losses into account, see [23]. Furthermore, Ferguson et al. [15] and Wang et al. [34] reconstruct the refractive index using measurements of the diffracted THz field based on the Helmholtz equation (so-called T-ray Diffraction Tomography, analogous to ultrasound tomography, see [9, 10]).

Due to the long wavelength of THz radiation compared to X-rays (for a frequency of $f = 0.1\,\text{THz}$, the wavelength is approx. $\lambda = 3\,\text{mm}$), wave phenomena need to be taken into account in the modeling of the measurement process. On the other hand, a more precise model leads to a computationally more intensive solution. Our task is to find a balance between both.

In the following we present a novel, hybrid algorithm for THz tomography. The algorithm is developed for a tomograph designed for medium-sized companies, which demands a short runtime. Because of that we search for an efficient solution of the inverse problem by considering only dominating effects.

The radiation from a THz source behaves ideally as a Gaussian beam and can be modeled by the wave equation or, if we are only interested in the intensity, by the Helmholtz equation. The transverse intensity profile is well approximated by Gaussian functions (see figure 1a). However, the solution of the Helmholtz equation is very time-consuming. The wave length is significantly smaller than in the case of acoustic waves, forcing a fine discretization of the domain of interest. This prevents an efficient solution with ultrasound tomography algorithms. Hence, our goal is a new algorithm not based on the solution of wave or Helmholtz equation, but still taking into account the main physical effects. These are primarily transmission, refraction at interfaces, reflection losses and the Gaussian beam profile (see figure 1b). In the following we will neglect the Gaussian beam profile for the sake of simplicity.

The THz tomography system used for this work provides intensity data, analogous to the conventional transmission tomography, as well as (delayed) travel times or path differences, as in ultrasound technology. The reconstruction algorithm described here uses travel time and transmission data simultaneously to reconstruct the material parameters refractive index and absorption coefficient. Therefore, we adapt the algebraic reconstruction technique (ART, see [16]) to our physical conditions by taking into account refraction at the interfaces of the object according to Snell's law and including the reflection losses given by the Fresnel equations. For this, we need some a priori information on the object's interfaces.

This approach is comparable to those in ultrasound CT and ultrasound vector field tomography, where reconstructions from travel time measurements are improved by considering ray paths which take deflection of the ray into account. In ultrasound CT, the ray paths are computed by solving the eikonal equation (ray tracing) [4, 30, 32]. This approach unfortunately requires a continuously differentiable refractive index and thus a smoothing of any discontinuities of the refractive index at interfaces. Furthermore, it is necessary to solve a nonlinear partial differential equation of first order. Ray tracing algorithms were successfully combined with algebraic reconstruction techniques (ART, SART) [1, 3, 12]. These algorithms work well, if discontinuities are smaller than $10 - 20\%$ refractive index deviation [2, 12]. In THz tomography, these deviations at interfaces are even higher compared to ultrasound tomography (about 50%). Therefore, refraction at interfaces can be assumed as a dominating effect in THz tomography.

In ultrasound vector field tomography, signals travel along geodesic curves of a Riemannian metric, which is associated with the refractive index according to Fermat's principle [31, 27]. The inverse problem consists of determining the refractive index from integrals along geodesics curves from ultrasound time-of-flight (TOF) measurements. In both, THz tomography and ultrasound vector field tomography, the ray path resp. geodesic curve depends on the unknown refractive index.

The algorithm presented here allows discontinuities in the refractive index and includes the change of direction of the rays at interfaces by a direct application of Snell's law.

The paper is organized as follows. In the next section we briefly recall the mathematical model for the 2D THz transmission and travel time tomography. Subsequently, the notation of the a priori given interfaces and a brief description of the physical model, especially the Fresnel equations and Snell's law, will be discussed. In Section 2.3 we derive a description of ray paths considering refraction. Section 3 deals with the development of the new algorithm, beginning with a brief revision of the conventional ART. Based on ART, we introduce the modified ART for THz tomography and its implementation. Eventually, the validation of the modified ART and its implementation are to be found in section 4 using synthetic as well as real measured data, comparing our algorithm with the filtered backprojection (FBP) and conventional ART. We conclude the paper with a summary of the main results and an outlook for future work and potential improvements.

## 2 The mathematical model of 2D THz tomography

We consider 2D THz transmission and travel time tomography with standard parallel scanning geometry. The main task is the reconstruction of an object characterized by the complex refractive index $\tilde{n} : \Omega \to \mathbb{C}$ with

$$\tilde{n}(x) = n(x) + i\kappa(x), \qquad x \in \Omega, \tag{2.1}$$

where $\Omega = \left\{x \in \mathbb{R}^2 : \|x\| < R\right\}$ with $R > 0$ the radius of the considered domain. The real part $n$ describes the optical path length of the material, whereas the imaginary part $\kappa$ models the material-dependent absorption. The transmission coefficient $\tau = I/I_0$ and the path difference

$d = c_0(T - T_0)$ are available as measured data, with $I_0$ the initial intensity, $I$ the intensity at the detector, $T$ the travel time with and $T_0$ without an object in the ray path and $c_0$ the speed of light. The real part of the complex refractive index is the quotient of the speed of light $c_0$ and the propagation speed $c_M$ inside the medium,

$$n(x) = \frac{c_0}{c_M(x)}, \qquad x \in \Omega,\ c_M > 0. \tag{2.2}$$

This means the (delayed) travel time is physically related to real part of $\tilde{n}$. The imaginary part

$$\kappa(x) = \alpha(x)\frac{c_0}{4\pi f}, \qquad x \in \Omega,\ f > 0, \tag{2.3}$$

describes the absorption of the wave by the absorption coefficient $\alpha$ in $\mathrm{cm}^{-1}$ and is connected to the transmission coefficient $\tau$. Furthermore, we assume that the complex refractive index vanishes outside the reconstruction region $\Omega$, i. e. $n(x) - 1 = 0$ and $\kappa(x) = 0$, if $x \notin \Omega$. Let $L$ be the propagation path of the THz radiation. The ratio of the transmitted intensity $I$ and the initial intensity $I_0$ is connected to the absorption coefficient $\alpha$ via

$$g_{\mathrm{abs}}(L) = \int_L \alpha(x)\,\mathrm{d}x = \ln\left(\frac{I_0}{I}\right) = \ln\left(\frac{1}{\tau}\right) \tag{2.4}$$

according to Lambert-Beer's law. The path difference is given by

$$g_{\mathrm{ref}}(L) = \int_L (n(x) - 1)\,\mathrm{d}x = d, \tag{2.5}$$

which follows from subtraction of the path in air with a refractive index of $n_0 = 1$, see [24].

Due to refraction at interfaces, THz rays do not necessarily propagate along straight lines. The rays are rather refracted at interfaces according to Snell's law. In case of a piecewise constant refractive index, the propagation path is continuous and consists of piecewise straight lines. We name the segments of a THz ray between two interfaces as "partial ray" $L_l \subseteq L$ with $l = 1, ..., \hat{K}+1$ and $\hat{K}$ the number of intersected interfaces. The first partial ray $L_1$ is parametrized as in X-ray CT until reaching the first interface, see [25, p. 41-42]. Let

$$\Gamma : \mathbb{R} \to \mathbb{R}^2, \qquad \Gamma(t) = s\omega(\varphi) + t\omega^{\perp}(\varphi) \tag{2.6}$$

be the parametrization of $L_1$ with distance $s \in \mathbb{R}$ from the origin, the angle $\varphi \in [0,\, 2\pi)$, $\omega(\varphi) = (\cos\varphi, \sin\varphi)^T$ and $\omega^{\perp} = (-\sin\varphi,\, \cos\varphi)^T$. Using $\Gamma$, the ray is represented by

$$L_1(\varphi, s) = \left\{\Gamma(t) :\ t \in \left[-\infty,\, t_1^{\mathrm{if}}(\varphi, s)\right]\right\} \tag{2.7}$$

with $t_1^{\mathrm{if}}(\varphi, s)$ the time of the incidence on the first interface (so-called "initial ray"). In X-ray CT, this parameter is usually set to $t_1^{\mathrm{if}} = \infty$. The full ray path depending on refraction is described in section 2.3. Therefore we first need to take a closer look at a suitable notation of the interfaces and afterwards we briefly describe the relevant physical laws.

## 2.1 Notation of interfaces

As mentioned before, we would like to use some a priori information. We postulate the knowledge of the object's interfaces, i. e. our a priori information contains positions and the normals of the interfaces of the object. This is quite a strong assumption, but in many cases the (approximate) location of some interfaces is actually known, for example from CAD drawings of the examined

object or preliminary testings with an X-ray CT. However, the interfaces of potential defects are unknown. Nevertheless, the knowledge of some interfaces already leads to better reconstructions.

**Definition 2.1.** An *interface* is a regular continuously differentiable and injective immersion $\Xi : [a, b] \to \Omega \subset \mathbb{R}^2$, fulfilling $\Xi'(\sigma) = \frac{d\Xi}{d\sigma} \neq 0$, $\forall \sigma \in [a, b]$.

The curve has a tangent and a normal $\mathfrak{n}$ at every point, because the first derivative $\Xi'$ is continuous and does not vanish. The tangent vector of $\Xi$ at $\sigma_0 \in [a,\, b]$ is given by

$$\Xi'(\sigma_0) = \left.\frac{d\Xi}{d\sigma}\right|_{\sigma=\sigma_0} = \Big(\xi_1'(\sigma_0),\, \xi_2'(\sigma_0)\Big)^T, \tag{2.8}$$

whereby we define the normal vector

$$\mathfrak{n}(\sigma_0) = \Big(-\xi_2'(\sigma_0),\, \xi_1'(\sigma_0)\Big)^T, \tag{2.9}$$

which we will need for Snell's law. Let $K \in \mathbb{N}$ be the number of known interfaces $\Xi_k$, $k = 1, ..., K$ of the object. Interfaces may touch or intersect each other as we often have to deal with non-smooth interfaces, e. g. rectangular objects. However, $\Xi'(\sigma)$ and hence the normal does not exist at corners. This case is handled by local smoothing. Let us assume, that

$$P := \bigcap_{\iota=1}^{\tilde{K}} \Xi_{k_\iota} \tag{2.10}$$

is the shared intersection of $\tilde{K} \in [1,\, K]$ different interfaces $\Xi_{k_\iota}$ with $k_\iota \in [1,\, K]\,, \iota = 1, ..., \tilde{K}$. Then $\sigma_{k_\iota} := \Xi_{k_\iota}^{-1}(P) \in [a_{k_\iota}, b_{k_\iota}]$ parametrizes the point of intersection on each interface and $\mathfrak{n}_{k_\iota}(\sigma_{k_\iota})$ are the corresponding normals for $\iota = 1, ..., \tilde{K}$. We now compute the normal in $P$ by averaging

$$\mathfrak{n} = \frac{\sum_{\iota=1}^{\tilde{K}} \mathfrak{n}_{k_\iota}(\sigma_{k_\iota})}{\left\|\sum_{\iota=1}^{\tilde{K}} \mathfrak{n}_{k_\iota}(\sigma_{k_\iota})\right\|}, \tag{2.11}$$

which can be interpreted as a mean orientation of the interfaces containing $P$. This approach sets a normal for the intersection, which occurs by a local smoothing of the corner $P$ (see figure 2). For $\tilde{K} = 1$ the normal vector is just normalized.

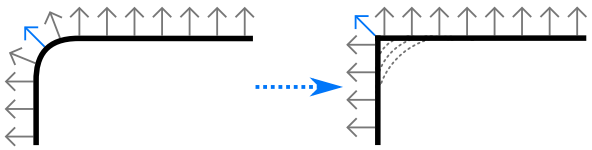

Figure 2: Dealing with corners: the calculated normal for the discontinuity corresponds to the normal of the smoothed interface at this point

## 2.2 Refraction and reflection losses

We follow the idea of Mukherjee et. al, see [23], who consider refraction and reflection losses for cylindrical objects with known refractive index for the reconstruction of the absorption coefficient. We generalize this approach for general objects with given interfaces, unknown $n$ and reconstruct both refractive index and absorption coefficient. The propagation of electromagnetic waves at an interface between two different media is influenced by refraction, reflection, diffraction and

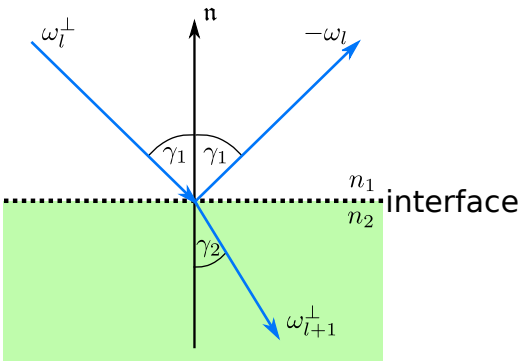


Figure 3: Snell's law with normal $\mathfrak{n}$ of the interface and direction vectors $\omega_l^\perp$, $\omega_{l+1}^\perp$ and $-\omega_l$ of the incident, refracted and reflected rays, $n_1 < n_2$

scattering. As stated before, we want to neglect diffraction and scattering. Let us consider the transition of a ray from a medium with refractive index $n_1$ into a medium with refractive index $n_2$. The change in the direction of propagation of the transmitted part of the THz ray can be calculated according to Snell's law

$$n_1 \sin \gamma_1 = n_2 \sin \gamma_2, \tag{2.12}$$

with the angle of incidence $\gamma_1$ and the angle of refraction $\gamma_2$ measured from the normal $\mathfrak{n}$ of the interface, see [6, p. 38 ff.]. When rays travel from a medium with a higher refractive index $n_1$ to one with a lower refractive index $n_2$, total reflection is possible for a sufficiently large $\gamma_1$. In this case, we have

$$\frac{n_1}{n_2} \sin \gamma_1 > 1, \qquad \text{for } n_1 > n_2 \tag{2.13}$$

and the radiation is fully reflected. The fraction of the incident radiation that is reflected at the interface can be described by the Fresnel equations, see [6, p. 38 ff.]. Reflection losses depend on the polarization of the incident wave, the angle of incident $\gamma_1$ and refraction $\gamma_2$ and the refractive indices. The reflectance of a ray that is polarized perpendicularly to the plane of incidence is given by

$$\rho = \left| \frac{E_r}{E_0} \right|^2 = \left| \frac{n_1 \cos \gamma_1 - n_2 \cos \gamma_2}{n_1 \cos \gamma_1 + n_2 \cos \gamma_2} \right|^2, \tag{2.14}$$

where $E_0$ resp. $E_r$ is the electric field amplitude of the incident resp. reflected partial ray. Analogous considerations exist also for parallel polarization. All other polarizations can be represented by a superposition of the linearly perpendicular and linearly parallel case.

## 2.3 Ray propagation considering refraction

The path of a THz ray $L$ up to reaching the first interface can be described by equation (2.7). The ray is refracted as it transitions into the next medium and the ray direction has to be recalculated according to Snell's law. We first have to determine the next intersection with an interface for each (refracted) partial ray $L_l$. The change in the direction of the ray is calculated in this intersection. Let the $l$-th partial ray $L_l$ be given by an angle $\varphi_l$ and a distance $s_l$, i .e. $L_l(\varphi_l, s_l) = \left\{\Gamma_l(t) = s_l\omega_l + t\omega_l^\perp : t \in \left[t_{l-1}^{\text{if}}, t_l^{\text{if}}\right]\right\}$. Now we calculate the intersections of $L_l$ with the interfaces and determine the parameter

$$t_l^{\text{if}}\left(\varphi_l, s_l\right) = \min_t \left\{ (t,\sigma) \in \left(t_{l-1}^{\text{if}}, \infty\right] \times [a_k, b_k] : \Gamma_l(t) = \Xi_k(\sigma),\, k = 1, ..., K \right\}, \tag{2.15}$$

which defines the nearest intersection with an interface in the direction of propagation with $l \geq 1$ and $t_0^{\text{if}} = -\infty$. Let $\Xi_{\tilde{k}}(\sigma)$, $\tilde{k} \in [1,\, K]$, be the nearest interface and $\tilde{\sigma}$ the parameter corresponding to $t_l^{\text{if}}$ in (2.15) of the intersection $\Xi_{\tilde{k}}(\tilde{\sigma}) = s_l\omega_l + t_l^{\text{if}}\omega_l^{\perp}$. We can determine the refractive indices for both sides of the interface, which we need for Snell's law, by

$$\begin{array}{llll} n_{l,1} := n\left(\Xi_{\tilde{k}}(\tilde{\sigma}) - \varepsilon\mathfrak{n}\right) & \text{and} & n_{l,2} := n\left(\Xi_{\tilde{k}}(\tilde{\sigma}) + \varepsilon\mathfrak{n}\right), & \text{for } \left\langle \omega_l^{\perp}, \mathfrak{n} \right\rangle \leq 0 \\ n_{l,1} := n\left(\Xi_{\tilde{k}}(\tilde{\sigma}) + \varepsilon\mathfrak{n}\right) & \text{and} & n_{l,2} := n\left(\Xi_{\tilde{k}}(\tilde{\sigma}) - \varepsilon\mathfrak{n}\right), & \text{for } \left\langle \omega_1^{\perp}, \mathfrak{n} \right\rangle > 0 \end{array} \tag{2.16}$$

with the normal $\mathfrak{n} := \mathfrak{n}(\tilde{\sigma})$ as in (2.11) and an appropriately small $\varepsilon > 0$. The angle of incidence $\gamma_{l,1}$ between the direction vector of the incident ray $\omega_l^{\perp}$ and normal $\mathfrak{n}$ (see figure 3) can be calculated by the scalar product in $\mathbb{R}^2$

$$\gamma_{l,1} = \arccos \left| \left\langle \omega_l^{\perp},\, \mathfrak{n} \right\rangle \right| \tag{2.17}$$

and the angle of the refracted ray can be obtained by

$$\gamma_{l,2} = \begin{cases} \pi - \gamma_{l,1}, & \text{for } n_{l,1} > n_{l,2} \wedge \gamma_{l,1} \geq \arcsin \frac{n_{l,2}}{n_{l,1}} \text{ (total reflection)}, \\ \arcsin \dfrac{n_{l,1} \sin \gamma_{l,1}}{n_{l,2}}, & \text{otherwise.} \end{cases} \tag{2.18}$$

The next direction vector $\omega_{l+1}$ can be easily derived by a rotation of $\omega_l := \omega\left(\varphi_l\right)$ around an angle $\theta = \pm\left(\gamma_{l,1} - \gamma_{l,2}\right)$ with the rotation matrix

$$R_\theta := \begin{pmatrix} \cos\theta & -\sin\theta \\ \sin\theta & \cos\theta \end{pmatrix} \tag{2.19}$$

see figure 4. The sign of $\theta$ depends on the orientation of the normal $\mathfrak{n}$ to the incident ray, see (2.20). After applying angle sum identities, the new angle $\varphi_{l+1}$ and the unit vector $\omega_{l+1}$ are computed by

$$\omega_{l+1}\left(\varphi_{l+1}\right) := \begin{cases} \omega(\overbrace{\gamma_{l,1} - \gamma_{l,2} + \varphi_l}^{=:\varphi_{l+1}}), & \text{for } \left\langle \omega_l^{\perp}, \mathfrak{n} \right\rangle < 0 \wedge \left\langle \omega_l^{\perp}, \mathfrak{n}^{\perp} \right\rangle \leq 0 \\ \omega(\gamma_{l,1} - \gamma_{l,2} + \varphi_l), & \text{for } \left\langle \omega_l^{\perp}, \mathfrak{n} \right\rangle > 0 \wedge \left\langle \omega_l^{\perp}, \mathfrak{n}^{\perp} \right\rangle \geq 0 \\ \omega(\gamma_{l,2} - \gamma_{l,1} + \varphi_l), & \text{for } \left\langle \omega_l^{\perp}, \mathfrak{n} \right\rangle \leq 0 \wedge \left\langle \omega_l^{\perp}, \mathfrak{n}^{\perp} \right\rangle > 0 \\ \omega(\underbrace{\gamma_{l,2} - \gamma_{l,1}}_{=:\theta} + \varphi_l), & \text{for } \left\langle \omega_l^{\perp}, \mathfrak{n} \right\rangle \geq 0 \wedge \left\langle \omega_l^{\perp}, \mathfrak{n}^{\perp} \right\rangle < 0 \end{cases}. \tag{2.20}$$

The next distance from the origin $s_{l+1}$ of partial ray $L_{l+1}$ follows directly from the intersection of the lines $(0 + u\omega_{l+1}) \cap \left(\Xi_{\tilde{k}}(\tilde{\sigma}) + t\omega_{l+1}^{\perp}\right)$ with parameters $t$ and $u$. We obtain with $\Xi_{\tilde{k}}(\tilde{\sigma}) := (\xi_1, \xi_2)^T$

$$s_{l+1} = \left| (0 + u\omega_{l+1}) \cap \left(\Xi_{\tilde{k}}(\tilde{\sigma}) + t\omega_{l+1}^{\perp}\right) \right| = \left| \cos\varphi_{l+1}\xi_1 + \sin\varphi_{l+1}\xi_2 \right|. \tag{2.21}$$

Consequently, the complete refracted ray path is given by the union

$$L\left(\varphi, s\right) := \bigcup_{l=1}^{\hat{K}+1} \left\{ \Gamma_l(t) :\, t \in \left[ t_{l-1}^{\text{if}},\, t_l^{\text{if}} \right] \right\} \tag{2.22}$$

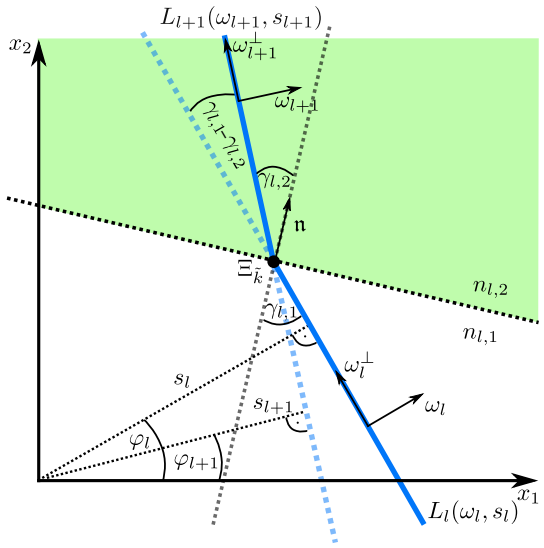


Figure 4: Snell's law and parametrization of a refracted THz ray

of all partial rays $L_l(\varphi_l, s_l)$ defined by (2.20) and (2.21) with an initial direction $\varphi = \varphi_1$ and distance $s = s_1$, $t_0^{\text{if}} = -\infty$, $t_{\hat{K}+1}^{\text{if}} = \infty$ and $\hat{K}$ the number of intersected interfaces. $\hat{K}$ is unknown at the beginning and depends on the ray path.

*Remark* 2.2. Please note that determining the ray paths depends on the refractive index $n$, which is the unknown quantity in our inverse problem. Therefore, the actual ray paths are also unknown in the beginning and are approached within the reconstruction process.

**Problem 2.3.** The inverse problem consists in determining the complex refractive index

$$\tilde{n}(x) = n(x) + i\alpha(x)\frac{c_0}{4\pi f}, \qquad x \in \Omega, \tag{2.23}$$

from the knowledge of the measured data $g_{\text{abs}}(\varphi_i, s_j) = \ln\left(\frac{1}{\tau(\varphi_i, s_j)}\right)$ and $g_{\text{ref}}(\varphi_i, s_j) = d(\varphi_i, s_j)$ of a parallel scanning geometry with (inital) angles $\varphi_i = \frac{2\pi(i-1)}{p}$ for $i = 1, ..., p$ and (initial) distances $s_j = \frac{R}{q}j$, for $j = -q, ..., q$. As we do not consider straight ray paths, we usually have $g_{\text{abs}}(-\varphi, s) \neq g_{\text{abs}}(\varphi, s)$ or $g_{\text{ref}}(-\varphi, s) \neq g_{\text{ref}}(\varphi, s)$ in contrast to X-ray CT. So the angles $\varphi_i$ should be evenly distributed over the interval $[0, 2\pi)$. Our task is to find the best possible approximation of $\tilde{n}$ satisfying

$$\int_{L(\varphi_i, s_j)} (n(x) - 1)\, \mathrm{d}x = g_{\text{ref}}(\varphi_i, s_j) \quad \text{and} \quad \int_{L(\varphi_i, s_j)} \alpha(x)\, \mathrm{d}x = g_{\text{abs}}(\varphi_i, s_j) \tag{2.24}$$

for $i = 1, ..., p$ and $j = -q, ..., q$.

# 3 Algorithm development

In the following, we develop a numerical algorithm for the calculation of the complex refractive index $\tilde{n}(x) = n(x) + i\alpha(x)\frac{c_0}{4\pi f}$. Since algorithms based on partial differential equations such as the wave equation are very time-consuming, an efficient reconstruction shall only consider dominating physical effects. Poor reconstructions, which arise from the application of conventional reconstruction algorithms from computed tomography to THz data, are often based on the missing consideration of refraction and reflection losses.

Therefore, we would like to modify ART for THz tomography. This is done by using a priori information (i. e. the knowledge of interfaces) and considering relevant physical laws (Snell's law and reflection losses according to Fresnel equations). This results in a method, which takes refraction as well as transmission into account and determines simultaneously the refractive index and the absorption coefficient from measurements of path difference and intensity data.

## 3.1 ART

Our method is based on the classical ART as described in e. g. [25, pp. 128, 137 ff.]. So we first give a brief overview of ART. The main idea behind of this method is the application of Kaczmarz's method to Radon's integral equation. We search for the solution of the system

$$\int_{L^\nu} f(x)\,\mathrm{d}x = g^\nu, \qquad \nu = 1, ..., N, \qquad x \in \Omega \tag{3.1}$$

where $L^\nu := L(\varphi_\nu, s_\nu)$ are straight lines, $f$ a function (refractive index $f = n - 1$ or absorption coefficient $f = \alpha$), $g^\nu := g(\varphi_\nu, s_\nu)$ the measured data (path difference or intensity data) and $N = p(2q + 1)$. Let

$$\Omega \subset \bigcup_{\mu=1}^{M} S_\mu \tag{3.2}$$

be a pixel discretization of the domain $\Omega$ with pixels $S_\mu$, $\mu = 1, ..., M$. We obtain a linear system by discretizing $f$ via

$$f(x) \approx \tilde{f}(x) = \sum_{\mu=1}^{M} f_\mu \chi_\mu(x), \qquad x \in \Omega, \tag{3.3}$$

with characteristic functions

$$\chi_\mu(x) = \begin{cases} 1, & \text{if } x \in S_\mu, \\ 0, & \text{otherwise.} \end{cases} \tag{3.4}$$

The integral is thus approximated by

$$\int_{L^\nu} f(x)\,\mathrm{d}x \approx \sum_{\mu=1}^{M} a_{\nu\mu} f_\mu \tag{3.5}$$

with $a_{\nu\mu} = \text{length}\,(L^\nu \cap S_\mu)$. Now, we define $a^\nu := (a_{\nu 1}, ..., a_{\nu M})^T \in \mathbb{R}^M$ and $F = (f_1, f_2, ..., f_M)^T \in \mathbb{R}^M$. Using the scalar product in $\mathbb{R}^M$, we obtain the discrete version of (3.1),

$$\langle a^\nu, F \rangle = g^\nu, \qquad \nu = 1, ..., N. \tag{3.6}$$

We solve this linear system by applying Kaczmarz's method to (3.6). The iteration then reads as

$$\begin{aligned} F^0 &:= \tilde{F}^r \\ F^\nu &= F^{\nu-1} + \lambda \frac{g^\nu - \langle a^\nu, F^{\nu-1} \rangle}{\|a^\nu\|_2^2} a^\nu, \qquad \nu = 1, \ldots, N \\ \tilde{F}^{r+1} &:= F^N \end{aligned} \tag{3.7}$$

with relaxation parameter $\lambda \in (0, 2)$, iteration index $r = 0, 1, 2, \ldots$, ray index $\nu$ and an arbitrary initial value $\tilde{F}^0$.

## 3.2 Modified ART

We modify ART taking refraction into account. This leads to a more sophisticated calculation of the projection matrix $A = (a_{\nu\mu})_{\nu=1,\ldots,N,\mu=1,\ldots,M}$. Furthermore, the consideration of Fresnel losses leads to a correction of the measured intensity data $g_{\text{abs}}$. Both linear systems (for path difference $d$ and transmission coefficient $\tau$) show a similar structure and can be solved simultaneously, using the same ray paths for both models, by applying Kaczmarz's method to get the complex refractive index.

### 3.2.1 Consideration of Fresnel losses

Reflection losses influence the measured transmission coefficient $\tau$ by reducing the intensity of the transmitted signal in addition to absorption losses. Neglecting reflection losses in the model will thus lead to a systematic error in the calculation of the absorption coefficient: the resulting values for $\alpha$ will be too high, as a larger absorption coefficient corresponds to smaller transmission coefficients. Therefore, our approach will be a correction of the measured intensity data, so that only absorption losses are considered for the reconstruction of the absorption coefficient. Mukherjee et al. [23] introduced this approach successfully for cylindric objects. We expand this approach to arbitrary interfaces and an initially unknown refractive index.

The reflection loss $\rho$ of a single interface is given by equation (2.14). For this purpose, we need the angle of incident and refraction, which are known from the calculation of the ray paths according to Snell's law, as well as the refractive indices on both sides of the interface, given by (2.16). Let $\hat{K} \in \mathbb{N}$ be the number of interfaces intersecting the ray path $L$ and $\rho_{k_\iota}$ be the reflection loss at interface $\Xi_{k_\iota}$ with $k_\iota \in [1, K], \iota = 1, \ldots, \hat{K}$. The emitted intensity is reduced due to the corresponding reflection losses by the factor

$$C_{\text{abs}} := \prod_{\iota=1}^{\hat{K}} (1 - \rho_{k_\iota}) . \tag{3.8}$$

In addition, the intensity of the ray is reduced by absorption losses according to Lambert-Beer's law

$$a = \exp\left( - \int_L \alpha \, \mathrm{d}x \right) . \tag{3.9}$$

As a consequence, the transmission coefficient

$$\tau = a \prod_{\iota=1}^{\hat{K}} (1 - \rho_{k_\iota}) \tag{3.10}$$

is measured by the receiver. We are now able to correct the measured transmission data (the right hand side of integral equation (2.4)) by

$$\tilde{g}_{\text{abs}} = \ln\left(\frac{I_0}{I}\right) = \ln\left(\frac{1}{a}\right) = \ln\left(\frac{1}{\tau}\prod_{\iota=1}^{\hat{K}}(1-\rho_{k_\iota})\right) \tag{3.11}$$

and obtain data that depends only on the absorption coefficient $\alpha$.

### 3.2.2 Consideration of the refracted ray path

A matrix entry $a_{\nu\mu}$ represents the length of the (refracted) ray $\nu$ in pixel $\mu$ as in conventional ART. In contrast to ART, we cannot calculate all entries $a_{\nu\mu}$ at once as the path itself is influenced by the material parameters. Instead, we have to determine first of all the parameter $t_l^{\text{if}}$ for partial ray $L_l^\nu(\varphi_l, s_l)$ (see section 2.3). Then, we calculate $a_{\nu\mu}$ until reaching the nearest interface, determine the new angle $\varphi_{l+1}$ according to Snell's law and the reflection loss $\rho_l$ for the current interface $\Xi_{\tilde{k}}$ according to Fresnel equations. Afterwards, these steps can be repeated for the next partial ray $L_{l+1}^\nu$, $l = 1, ..., \hat{K}$ and $\nu = 1, ..., N$. A pseudo code for calculating the matrix $A$ and the reflection losses is given in algorithm 1.

**Algorithm 1** Calculating matrix $A$ and the corrected $\tilde{g}_{\text{abs}}$

**for** $\nu = 1$ to $N$ **do**
  $\rho = 0,\ t_0^{\text{if}} = -\infty,\ t_1^{\text{if}} = 0,\ l = 1$
  **while** $t_l^{\text{if}} < \infty$ **do**
    Calculate $t_l^{\text{if}}$ by (2.15)
    Calculate $a_{\nu\mu} = \text{length of } (L_l^\nu \cap S_\mu)$ for $t \in \left[t_{l-1}^{\text{if}}, t_l^{\text{if}}\right]$
    **if** $t_l^{\text{if}} < \infty$ **then**
      Calculate partial ray $L_{l+1}^\nu(\varphi_{l+1}, s_{l+1})$ by (2.20) and (2.21)
      Calculate reflection losses $\rho_l^\nu$ at $\Xi_{\tilde{k}}$ by (2.14)
      $l = l + 1$
    **end if**
  **end while**
  $\hat{K}^\nu = l - 1$;
  Calculate $C_{\text{abs}}^\nu = \prod_{l=1}^{\hat{K}^\nu}(1-\rho_l^\nu)$
**end for**
$\tilde{g}_{\text{abs}}^\nu = \ln\left(\frac{C_{\text{abs}}^\nu}{\tau^\nu}\right),\ \nu = 1, ..., N$
**return** $A, \tilde{g}_{\text{abs}}$

The reconstruction of $\text{Re}(\tilde{n}) = n$ has a direct influence on the reconstruction of the absorption coefficient $\alpha$, because the reflection losses are calculated by using the refractive indices of the materials that share the interface. The remaining steps are identical to ART. We can use the same matrix $A$ for the reconstruction of both $n-1$ and $\alpha$ and thus the calculation of $F_{\text{ref}}^r$ and $F_{\text{abs}}^r$ takes place in the same loop, speeding up the reconstruction significantly. In the worst case, the complex refractive index is completely unknown and the initial guess is the complex refractive index of air, meaning $F_{\text{ref}}^0 = F_{\text{abs}}^0 = 0$. In this case it makes sense to perform consecutively several applications of Kaczmarz's method and use their approximations for an update of the ray paths, calculating a new matrix $A$ and correction value $C_{\text{abs}}$ before the next iteration. This means, we calculate the first approximation by conventional ART without considering the interfaces and reflection losses and then the next steps follow with modified ART based on this approximation. This update of ray paths based on an initial guess like $F_{\text{ref}}^0 = 0$ was discussed before in [19] and [30], where it was used in the context of reconstructions based on the eikonal equation.

### 3.2.3 Numerical scheme

Let $\Psi$ be the number of applications of Kaczmarz's method. We can set the number of iterations $\psi = \left(r^1_{\text{stop}}, ..., r^\Psi_{\text{stop}}\right)$ and the relaxation parameters for the refractive index $\lambda_{\text{ref}} = \left(\lambda^1_{\text{ref}}, ..., \lambda^\Psi_{\text{ref}}\right)$ and absorption coefficient $\lambda_{\text{abs}} = \left(\lambda^1_{\text{abs}}, ..., \lambda^\Psi_{\text{abs}}\right)$ for each iteration. An appropriate choice of $\psi$ is important, due to the well-known phenomenon of the semiconvergence of iterative methods for inverse problems. The stopping indices $r^i_{\text{stop}}$, $i = 1, ..., \Psi$, are the respective regularization parameters of the modified ART and have to be chosen adequately (e. g. by the discrepancy principle, see [11]). The algorithm for the calculation of an approximation of the complex refractive index based on THz data is shown in algorithm 2. Altogether this leads to the numerical scheme for the modified algebraic reconstruction technique as outlined in figure 5.

**Algorithm 2** Modified ART for calculating $\tilde{n} = n + i\kappa$

Inital values $\tilde{F}^{0,1}_{\text{ref}}$, $\tilde{F}^{0,1}_{\text{abs}}$
**for** $i = 1$ to $\Psi$ **do**
  Calculate $A^i\left(\tilde{F}^{0,i}_{\text{ref}}\right)$ and $\tilde{g}_{\text{abs}}\left(\tilde{F}^{0,i}_{\text{ref}}\right)$ by algorithm 1
  $r = 0$
  **while** $r \leq r^i_{\text{stop}}$ **do**
    $F^0_{\text{ref}} = \tilde{F}^{r,i}_{\text{ref}}$, $F^0_{\text{abs}} = \tilde{F}^{r,i}_{\text{abs}}$
    **for** $\nu = 1$ to $N$ **do**
      $$F^\nu_{\text{ref}} = F^{\nu-1}_{\text{ref}} + \lambda^i_{\text{ref}} \frac{g^\nu_{\text{ref}} - \left\langle a^\nu, F^{\nu-1}_{\text{ref}} \right\rangle}{\|a^\nu\|^2_2} a^\nu$$
      $$F^\nu_{\text{abs}} = F^{\nu-1}_{\text{abs}} + \lambda^i_{\text{abs}} \frac{\tilde{g}^\nu_{\text{abs}} - \left\langle a^\nu, F^{\nu-1}_{\text{abs}} \right\rangle}{\|a^\nu\|^2_2} a^\nu$$
    **end for**
    $\tilde{F}^{r+1}_{\text{ref}} = F^N_{\text{ref}}$, $\tilde{F}^{r+1}_{\text{abs}} = F^N_{\text{abs}}$
    $r = r + 1$
  **end while**
  $\tilde{F}^{0,i+1}_{\text{ref}} = F^N_{\text{ref}}$, $\tilde{F}^{0,i+1}_{\text{abs}} = F^N_{\text{abs}}$
**end for**
**return** $\tilde{n} \approx \left(1 + \tilde{F}^{0,\Psi+1}_{\text{ref}}\right) + i\left(\tilde{F}^{0,\Psi+1}_{\text{abs}} \frac{c_0}{2\omega}\right)$

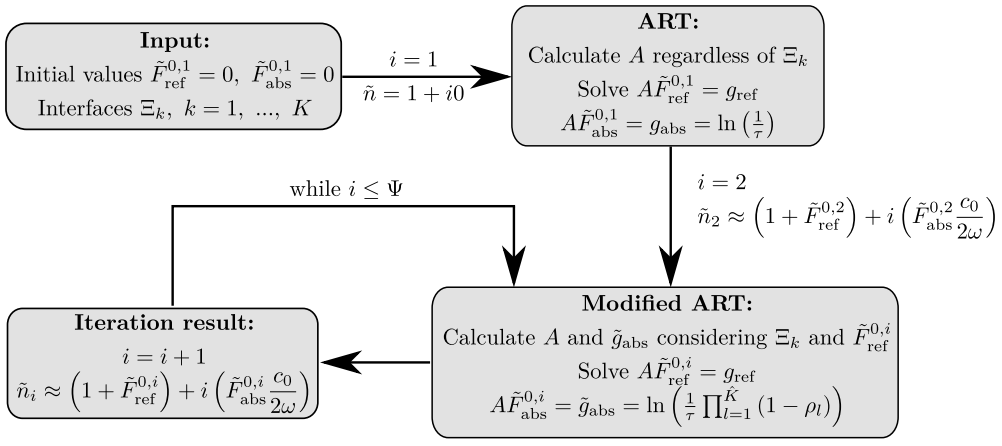


Figure 5: Numerical scheme of the modified ART

# 4 Numerical experiments and results

In this section we would like to validate the modified ART using both synthetic and real measured data. The results show an improvement of the reconstruction obtained by the proposed technique in comparison to conventional CT methods. The complex refractive index can be reconstructed in more detail and with smaller errors by applying the new algorithm.

First of all we take a look at reconstructions with synthetic and noisy data. Afterwards, we compare the results obtained by modified ART with those resulting from FBP and conventional ART on the basis of real measured data. Synthetic and real measured data were both recorded for $p = 360$ initial angles and 141 distances (meaning $q = 70$). Therefore one data set consists of $N = 50760$ measurements. Furthermore, the number of iterations $\psi$ and the number of applications of Kaczmarz's methods $\Psi$, i. e. the regularization parameters, were chosen without a parameter-choice method for the sake of simplicity. The iterations are just terminated when further iterations show no significant improvement, but not yet divergence.

Additionally, we use the a priori information on the position of the interfaces to reset the refractive index outside the object to $n - 1 = 0$ before each Kaczmarz's method. Thus the angles of incidence and refraction are calculated more accurately, as the ray is broken at an actual discontinuity of the refractive index. The initial values $\tilde{F}^{0,1}_{\text{ref}} = \tilde{F}^{0,1}_{\text{abs}} = 0$ are used for all reconstructions, therefore the first iteration is equivalent to conventional ART.

## 4.1 Synthetic data

The first numerical example concerns a circle with a radius of 50 mm, a refractive index of $n = 1.4$ and an absorption coefficient of $\alpha = 0.05\,\text{cm}^{-1}$ containing an embedded rectangle with dimensions of $25\,\text{mm} \times 20\,\text{mm}$ and $n = 1.7$, $\alpha = 0.25\,\text{cm}^{-1}$. Uniformly distributed noise is added respectively to the synthetic transmission coefficient and path difference data, such that the obtained noisy data $g^\varepsilon$ fulfills

$$\|g - g^\varepsilon\|_2 \,/\, \|g\|_2 \leq 0.05 \tag{4.1}$$

in both cases. As there is no information about $\tilde{n}$, we perform several applications of Kaczmarz's

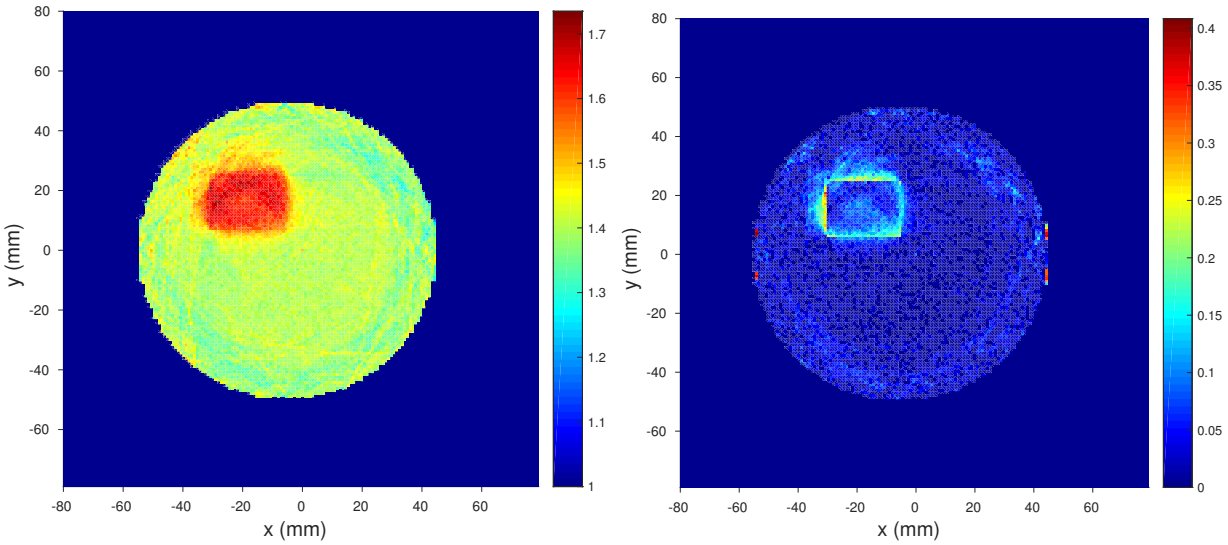


(a) Refractive index $n(x)$, $x \in \Omega$ (b) Absolute error

Figure 6: Reconstruction of the refractive index based on synthetic data

method for the reconstruction as described in section 3.2.3. Here we used $\Psi = 5$ iterations with the following parameters:

$$\begin{aligned} \psi &= (3,\ 3,\ 5,\ 7,\ 5) \\ \lambda_{\text{ref}} &= (0.01,\ 0.01,\ 0.006,\ 0.002,\ 0) \\ \lambda_{\text{abs}} &= (0.002,\ 0.004,\ 0.004,\ 0.004,\ 0.003) \end{aligned} \tag{4.2}$$

We perform only a reconstruction of the absorption coefficient $\alpha$ in last iteration ($\lambda^5_{\text{ref}} = 0$). This approach is reasonable in so far as we use the approximation of the previous iteration step of the refractive index $n$ for calculating the reflection losses for the reconstruction of $\alpha$. Therefore, we can expect an improvement of $\alpha$ in an additional iteration step. Figures 6 and 7 show the

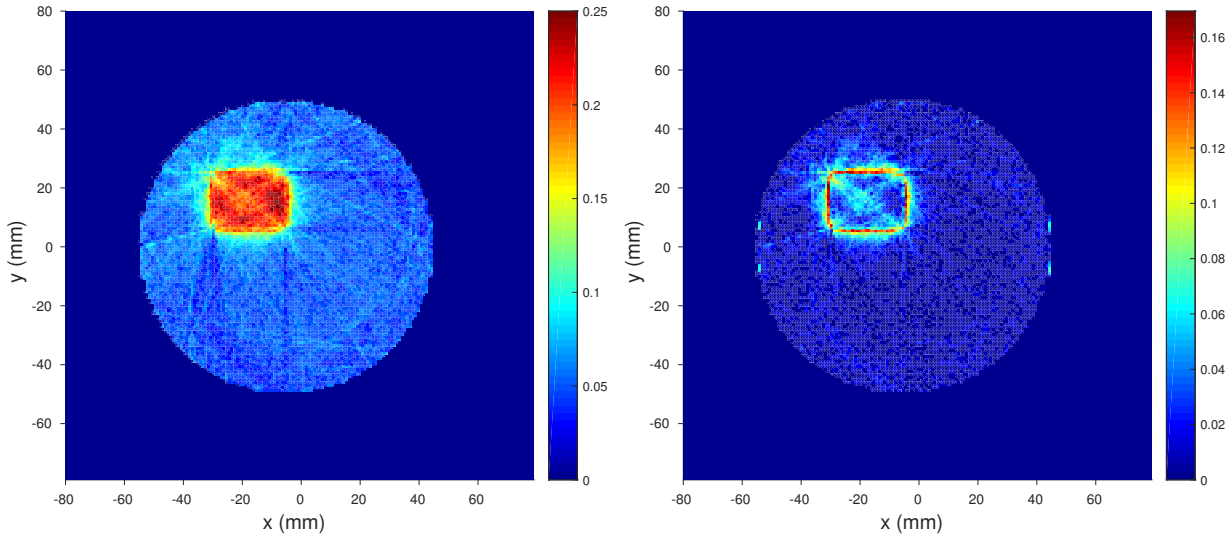


(a) Absorption coefficient $\alpha(x)$, $x \in \Omega$ (b) Absolute error

Figure 7: Reconstruction of the absorption coefficient based on synthetic data

reconstructions of the refractive index and the absorption coefficient with the modified ART. The results are good in spite of the large jump discontinuities of the refractive index. The absolute error is small in large parts of the object (see figures on the right), whereas the the biggest local errors appear near the interfaces and corners. Hereby, the prerequisite is ensured that modified ART provides correct results with synthetic data. As we now have to deal with ray paths that can be arbitrary refracted at interfaces, it is possible that some pixels are less frequently intersected by the ray paths than others, which causes additional artifacts.

## 4.2 Comparison with conventional reconstruction methods using real data

The next step is to compare modified ART with conventional ART and FBP based on real measured data. In this context, we first give a brief description of the used THz tomograph and then move on to the reconstructions.

### 4.2.1 THz tomography system

The measured data were acquired at *SKZ*[1]. A THz tomography system was designed, which works on the basis of the FMCW (Frequency Modulated Continuous Wave) principle. Here

[1] The German Plastics Center in Würzburg, http://www.skz.de/

the frequency of the THz signal is a sawtooth wave in the range of 70 to 110 GHz and allows measurements of intensity and phase. The latter results in the delayed travel time or path difference data. Dispersion can be neglected in this operating frequency range and the complex refractive index can be assumed to be constant [22, 28]. Thus the transmission coefficient and the path difference are averaged over this frequency band. The optical system consists of two lenses for each receiver and transmitter and is similar to the architecture of a Kepler telescope. The Gaussian beam is focused on the object with a beam waist of about 8 mm.

*Remark* 4.1. The generation of synthetic data always provides suitable values $g_{\text{abs}}$ and $g_{\text{ref}}$, regardless of how strong the rays are refracted. However, the THz system uses just one emitter and one detector, and in the case of strong refraction the transmitted ray may miss the detector, resulting in a transmission coefficient of $\tau = 0$. Better results can often be achieved by sorting out measured data of rays with $\tau \leq \varepsilon_{\text{miss}}$ and $\varepsilon_{\text{miss}}$ sufficiently small, meaning neglecting them completely for the iterations. It must be taken into account that this case also occurs for strong absorbers and then leads to a distortion of the reconstruction results.

### 4.2.2 Block with multiple refractive indices

The next step is to validate our modified ART with a more complex object and real measured data. Furthermore, we would like to compare the filtered backprojection, conventional ART and modified ART. For this purpose a test object consisting of different plastic blocks with different refractive indices that where glued together forming a block was scanned. Figure 8 shows the measures and the refractive indices of the object. The conventional ART no longer achieves

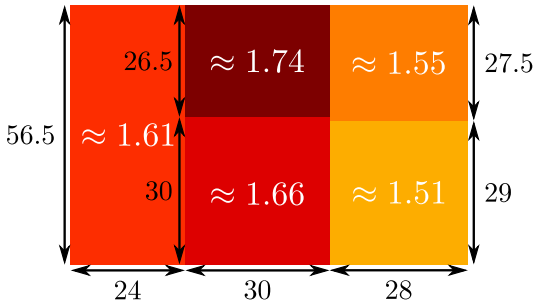


Figure 8: Refractive indices and proportions (in mm) of the glued-together block

significant improvements after 15 iterations with $\lambda_{\text{ref}} = 0.005$. The results of modified ART are obtained with $\psi = (3, 3, 5, 12)$ and $\lambda_{\text{ref}} = (0.005, 0.01, 0.0075, 0.003)$. THz rays resulting in transmission coefficients with $\tau \leq 0.05$ are ignored in both algebraic methods. Furthermore, we used the filtered backprojection with the Shepp-Logan filter and $\varepsilon_{\text{miss}} = 0$. The application of FBP to THz data leads to a very bad reconstruction (see figure 9) with very high values of $n$ at the outer interfaces. The shape of the object is completely lost and cannot be reconstructed. The reconstruction of the conventional ART is slightly better (see figure 10). But the outer shape of the object also appears too curved and the reconstruction of the refractive index produces very high values especially around the interfaces.

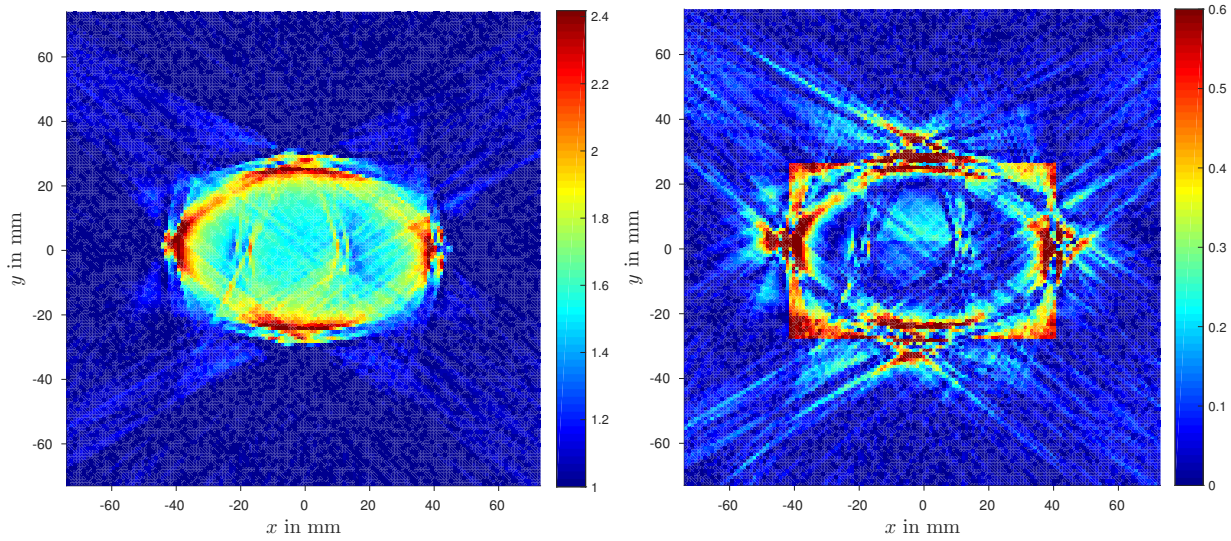


(a) Refractive index $n(x)$, $x \in \Omega$ (b) Absolute error

Figure 9: Filtered backprojection: reconstruction of the refractive index with real measured data

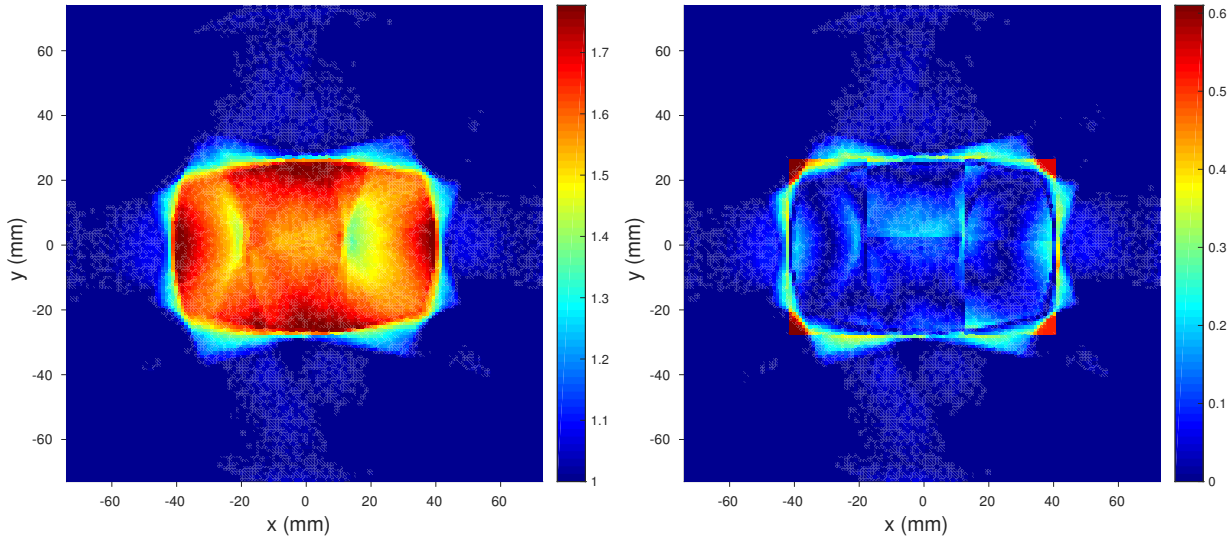


(a) Refractive index $n(x)$, $x \in \Omega$ (b) Absolute error

Figure 10: ART: reconstruction of the refractive index with real measured data

Conversely, the reconstruction with the modified ART is much better, see figure 11, and good results can also be achieved for more complex objects. The modified ART outperforms the conventional methods FBP and ART, especially around corners, regarding shape and size of the refractive index. This is also evident from the comparison of the three methods regarding the absolute error (see respective figures on the right-hand side).

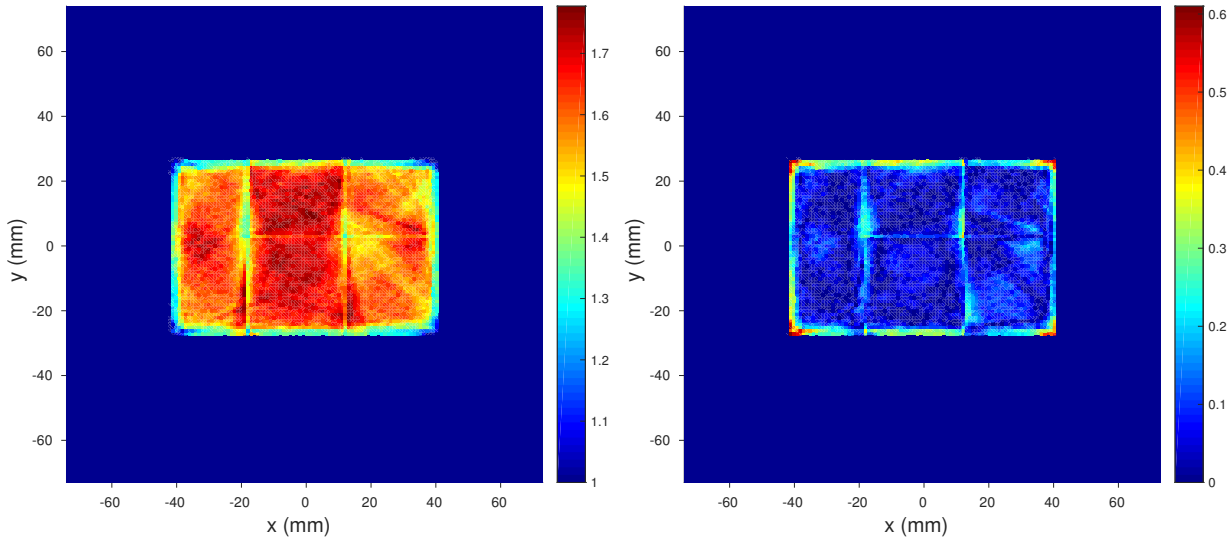


(a) Refractive index $n(x)$, $x \in \Omega$ (b) Absolute error

Figure 11: Modified ART: reconstruction of the refractive index with real measured data

The absolute error of the modified ART is almost everywhere smaller. The biggest deviations appear again at the corners and interfaces. Consequently, our modified ART can reconstruct more complex objects with smaller errors and in more detail, while the individual blocks are hardly detectable with ART. The differentiation of the various plastics is difficult with modified ART as well, because the values of the refractive indices are close to each other. But we can clearly distinguish between polyamide (middle top, with the highest refractive index) and polyethylene (right bottom, with the lowest refractive index). Finally, the reconstructions with modified ART are clearly superior to those of FBP and ART, showing that refraction and reflection losses play an important role in THz tomography.

## 5 Conclusion and future work

In this paper, we have presented a new, efficient reconstruction algorithm for THz tomography and have validated it with the help of synthetic and real measured data. Our modified ART takes refraction and reflection losses into account and reconstructs the complex refractive index based on path difference and transmission coefficient measurements. Therefore we use a refracted ray path according to Snell's law. Furthermore, modified ART is a hybrid algorithm exploiting two different tomographic principles (travel time and transmission tomography) and the respective data simultaneously.

Numerical experiments show that the reconstruction of material parameters and interfaces provide more accurate results than conventional CT algorithms like ART. We have already pointed out in the introduction that finding a balance between an efficient reconstruction and a detailed modeling is important. Hence, the modified ART considers only the main physical effects like refraction, absorption and reflection losses. The advantage of this approach is that we can avoid the expensive solution of partial differential equations like wave equation or Helmholtz equation. As we neglect further physical effects in our modeling, our proposed method has the following limitations: Since we do not consider diffraction effects, objects containing small, non-absorbing defects that lead to strong diffraction are poorly reconstructed. Although the first results are promising, the reconstruction algorithm for THz tomography can be improved by the following

approach: An important property of THz radiation is the propagation according to Gaussian optics. At this point, we neglect this physical property, suggesting the consideration of the Gaussian beam profile as a promising next step. Taking into account the Gaussian beam profile, we might also consider cases in which only a part of the transmitted beam hits the receiver and thus improve the reconstruction of the absorption coefficient.

To reduce the time required for reconstruction by parallelization, using the simultaneous algebraic reconstruction technique (SART, [5]) or more general block algebraic iterative methods (see e. g. [33]) is conceivable. Since the modifications to conventional ART concern only the matrix $A$ and the data $g_{\text{abs}}$, the iteration of e. g. SART is directly applicable, too.

## Acknowledgments

This project was funded by The German Federation of Industrial Research Associations (AiF) under 457 ZN which is gratefully acknowledged by the authors.

## References

[1] A. H. Andersen, *Tomography transform and inverse in geometrical optics*, J. Opt. Soc. Am. A, 4 (1987), pp. 1385–1395.

[2] ——, *A ray tracing approach to restoration and resolution enhancement in experimental ultrasound tomography*, Ultrasonic Imaging, 12 (1990), pp. 268–291.

[3] ——, *Ray tracing for reconstructive tomography in the presence of object discontinuity boundaries: A comparative analysis of recursive schemes*, J. Acoust. Soc. Am., 89 (1991), pp. 574–582.

[4] A. H. Andersen and A. C. Kak, *Digital ray tracing in two dimensional refractive fields*, J. Acoust. Soc. Am., 72 (1982), pp. 1593–1606.

[5] ——, *Simultaneous algebraic reconstruction technique (SART): A superior implementation of the ART algorithm*, Ultrasonic Imaging, 6 (1984), pp. 81–94.

[6] M. Born and E. Wolf, *Principles of optics: electromagnetic theory of propagation, interference and diffraction of light*, Pergamon Press, 4 ed., 1970.

[7] A. Brahm, M. Kunz, S. Riehemann, G. Notni, and A. Tünnermann, *Volumetric spectral analysis of materials using terahertz-tomography techniques*, Applied Physics B: Lasers and Optics, 100 (2010), pp. 151–158.

[8] A. Brahm, A. Wilms, M. Tymoshchuk, C. Grossmann, G. Notni, and A. Tünnermann, *Optical effects at projection measurements for terahertz tomography*, Optics & Laser Technology, 62 (2014), pp. 49–57.

[9] D. Colton, J. Coyle, and P. Monk, *Recent developments in inverse acoustic scattering theory*, SIAM Review, 42 (2000), pp. 369–414.

[10] D. Colton and R. Kress, *Inverse Acoustic and Electromagnetic Scattering Theory*, Applied mathematical sciences, Springer New York, 3 ed., 2013.

[11] M. Defrise and C. De Mol, *A note on stopping rules for iterative regularization methods and filtered SVD*, Inverse Problems: An Interdisciplinary Study, P.C. Sabatier, ed., Academic Press, New York, (1987), pp. 261–268.

[12] F. Denis, O. Basset, and G. Gimenez, *Ultrasonic transmission tomography in refracting media: reduction of refraction artifacts by curved-ray techniques*, IEEE Transactions on Medical Imaging, 14 (1995), pp. 173–188.

[13] B. Ewers, A. Kupsch, A. Lange, B. Müller, A. Hoehl, R. Müller, and G. Ulm, *Terahertz spectral computed tomography*, in IRMMW-THz 2009. 34th International Conference on Infrared, Millimeter, and Terahertz Waves, Sept 2009, pp. 1–2.

[14] B. Ferguson, *Three Dimensional T-ray Inspection Systems*, PhD thesis, University of Adelaide, 2004.

[15] B. Ferguson, S. Wang, D. Gray, D. Abbot, and X.-C. Zhang, *T-ray computed tomography*, Optics Letters, 27 (2002), pp. 1312–1314.

[16] R. Gordon, R. Bender, and G. T. Herman, *Algebraic reconstruction techniques (ART) for three-dimensional electron microscopy and X-ray photography*, Journal of Theoretical Biology, 29 (1970), pp. 471 – 481.

[17] J. Guillet, B. Recur, L. Frederique, B. Bousquet, L. Canioni, I. Manek-Hönninger, P. Desbarats, and P. Mounaix, *Review of terahertz tomography techniques*, Journal of Infrared, Millimeter, and Terahertz Waves, 35 (2014), pp. 382–411.

[18] M. Jewariya, E. Abraham, T. Kitaguchi, Y. Ohgi, M. Minami, T. Araki, and T. Yasui, *Fast three-dimensional terahertz computed tomography using real-time line projection of intense terahertz pulse*, Opt. Express, 21 (2013), pp. 2423–2433.

[19] S. Johnson, J. Greenleaf, W. Samayoa, F. Duck, and J. Sjostrand, *Reconstruction of three-dimensional velocity fields and other parameters by acoustic ray tracing*, in Ultrasonics Symposium, 1975, pp. 46–51.

[20] A. Kak, *Computerized tomography with X-ray, emission, and ultrasound sources*, Proceedings of the IEEE, 67 (1979), pp. 1245–1272.

[21] N. Krumbholz, T. Hochrein, N. Vieweg, T. Hasek, K. Kretschmer, M. Bastian, M. Mikulics, and M. Koch, *Monitoring polymeric compounding processes inline with THz time-domain spectroscopy*, Polymer Testing, 28 (2009), pp. 30–35.

[22] J. W. Lamb, *Miscellaneous data on materials for millimetre and submillimetre optics*, International Journal of Infrared and Millimeter Waves, 17 (1996), pp. 1997–2034.

[23] S. Mukherjee, J. Federici, P. Lopes, and M. Cabral, *Elimination of Fresnel reflection boundary effects and beam steering in pulsed terahertz computed tomography*, Journal of Infrared, Millimeter, and Terahertz Waves, 34 (2013), pp. 539–555.

[24] F. Natterer, *The Mathematics of Computerized Tomography*, Classics in Applied Mathematics, John Wiley & Sons Ltd and B. G. Teubner, Stuttgart, 1986.

[25] F. Natterer and F. Wübbeling, *Mathematical methods in image reconstruction*, SIAM Monographs on Mathematical Modeling and Computation, (2001), pp. 1–207.

[26] K. L. Nguyen, M. L. Johns, L. Gladden, C. H. Worrall, P. Alexander, H. E. Beere, M. Pepper, D. A. Ritchie, J. Alton, S. Barbieri, and E. H. Linfield, *Three-dimensional imaging with a terahertz quantum cascade laser*, Opt. Express, 14 (2006), pp. 2123–2129.

[27] T. Pfitzenreiter and T. Schuster, *Tomographic reconstruction of the curl and divergence of 2d vector fields taking refractions into account*, SIAM Journal on Imaging Sciences, 4 (2011), pp. 40–56.

[28] R. Piesiewicz, C. Jansen, S. Wietzke, D. Mittleman, M. Koch, and T. Kürner, *Properties of building and plastic materials in the THz range*, International Journal of Infrared and Millimeter Waves, 28 (2007), pp. 363–371.

[29] B. Recur, J. P. Guillet, I. Manek-Hönninger, J. C. Delagnes, W. Benharbone, P. Desbarats, J. P. Domenger, L. Canioni, and P. Mounaix, *Propagation beam consideration for 3d THz computed tomography*, Opt. Express, 20 (2012), pp. 5817–5829.

[30] H. Schomberg, *An improved approach to reconstructive ultrasound tomography*, Journal of Physics D: Applied Physics, 11 (1978), pp. L181–L185.

[31] U. Schröder and T. Schuster, *An iterative method to reconstruct the refractive index of a medium from time-of-flight measurements*, preprint, arXiv:1510.06899, (2015).

[32] A. Smith, M. Goldberg, and E. Liu, *Numerical ray tracing in media involving continuous and discrete refractive boundaries*, Ultrasonic Imaging, 2 (1980), pp. 291–301.

[33] H. H. B. Sørensen and P. C. Hansen, *Multicore performance of block algebraic iterative reconstruction methods*, SIAM Journal on Scientific Computing, 36 (2014), pp. C524–C546.

[34] S. Wang and X.-C. Zhang, *Pulsed terahertz tomography*, Journal of Physics D: Applied Physics, 37 (2004), pp. R1–R36.